ACS Photonics

Article

pubs.acs.org/journal/apchd5

Ce^{3+}-Sensitized $GdPO_4$:Tb^{3+} Nanorods: An Investigation on Energy Transfer, Luminescence Switching, and Quantum Yield

Niroj Kumar Sahu,[†] N. Shanta Singh,[†] R. S. Ningthoujam,*[,‡] and D. Bahadur*[,†]

[†]Department of Metallurgical Engineering and Materials Science, Indian Institute of Technology Bombay, Mumbai 400 076, India

[‡]Chemistry Division, Bhabha Atomic Research Center, Mumbai 400 085, India

Supporting Information

ABSTRACT: Herein we report the enhanced green emission from Tb^{3+}-doped $GdPO_4$ nanorods sensitized with Ce^{3+}. The increase in the rate of nonradiative transition processes in sensitizer due to efficient energy transfer to activator is realized from steady-state and dynamic luminescence studies. Luminescence quenching due to cross relaxation is least significant up to 20 at. % Ce^{3+} and 7 at. % Tb^{3+} concentration. The quantum yield of the sample with maximum luminescence, i.e., $GdPO_4$:Tb^{3+} (5 at. %)/Ce^{3+} (7 at. %), is found to be 28%. Also, samples are readily redispersible in water and could be easily incorporated in polymer-based films that show strong green light emission under UV excitation. The luminescence switching (ON and OFF) behavior is examined using alternately an oxidizing agent ($KMnO_4$) and then a reducing agent (ascorbic acid) through a redox reaction (Ce^{3+}/Ce^{4+}). Both $GdPO_4$:Tb^{3+} and $GdPO_4$:Tb^{3+}/Ce^{3+} are observed to be paramagnetic.

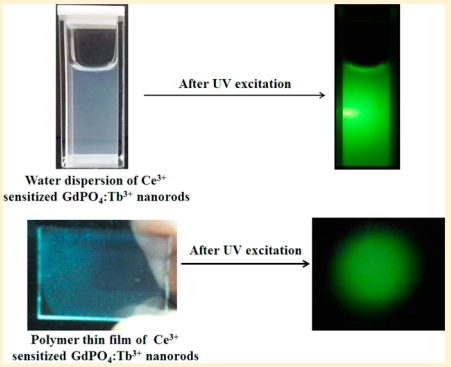

KEYWORDS: *photoluminescence, energy transfer, redispersion, polymer film, magnetic behavior, optical switching*

During the past decades, remarkable progress has been made in exploring varieties of physical, chemical, and biological applications of nanomaterials.[1−7] Among many of the nanomaterials, luminescent nanoparticles are potentially useful for versatile applications including display and lighting devices, lasers, optical amplifiers, catalysis, and bioimaging.[6−10] In particular, nanoparticles doped with lanthanide ions are significant for technological applications in the field of optoelectronics, sensing, and bioimaging due to a large Stokes shift.[11−17] Generally the nanoparticles have lower luminescence quantum yields and shorter fluorescence lifetime than their bulk counterparts due to their large number of defects present on the surface, such as unsaturated bonds, surface-adsorbed ions/molecules (H_2O, CO_3^{2-}), impurities, ligands, and an inhomogeneous distribution of lanthanide (Ln) ions. Owing to the presence of these defects on the surface of the nanoparticles, luminescence contributed by the inhomogeneous Ln^{3+} ions present on the surface of the particles is weakened. Thus, they act as the quencher in luminescence.[18−24] Wang et al.[18] systematically have shown the quenching of Ln^{3+} luminescence in the smaller nanoparticles (~10 nm) compared to the bigger size particles (~25 nm) due to the presence of more surface defects on smaller nanoparticles. These surface defects can be minimized by forming core−shell structures or annealing.[18,19,25] In our recent study on $GdPO_4$:Eu^{3+} nanorods,[19] the luminescence intensity of the sample increases with annealing at 500 and 900 °C, which is due to the removal of water in the lattice, as predicted by the thermogravimetric analysis and increase in crystallinity. This improvement in the crystallinity or reduction in the surface defect per gram of sample with annealing helps in the enhancement of the luminescence of the Ln^{3+} (Ln = Eu). For example, the presence of water over the surface of the nanoparticles can quench luminescence intensity of the Ln^{3+} because the second or third overtones of the fundamental frequency of water (O−H ≈ 3600 cm^{-1}) can match the energy gap between excited and ground states of Ln^{3+}, and thus, multiphonon relaxation occurs leading to a more nonradiative rate than radiative rate. However, lanthanide-doped rare-earth (RE) oxide nanoparticles possess several advantages. These include lower screen loading in display devices, high screen resolution, stable dispersion due to functionalized surface, easy encapsulation on porous materials such as silica, and easy processing for polymer-based film.[17,20,26]

ABO_4 (A = RE, B = P, Mo, V)-type rare-earth oxides including phosphates,[27−29] molybdates,[30] and vanadates[31−33] are suitable host materials for lanthanide activators where the efficient energy transfer to excited states of activators is possible for the enhancement of the luminescence. In this prospect, the gadolinium ion (Gd^{3+}), having a large absorption cross section due to the $^8S_{7/2}\rightarrow{}^6I_{11/2}$ transition in the ultraviolet (UV) region, has the advantage of energy transfer from Gd^{3+} to activator ions (Tb^{3+}, Eu^{3+}, Sm^{3+}, etc.). Adding a sensitizer such as Ce and Bi becomes important for further enhancement in luminescence efficiency by an effective energy transfer process through the sensitizer. In particular, sensitization with Ce^{3+} in $GdPO_4$:Tb^{3+} (termed $GdPO_4$:Tb^{3+}/Ce^{3+}) plays a crucial role in

Received: September 5, 2013
Published: March 20, 2014

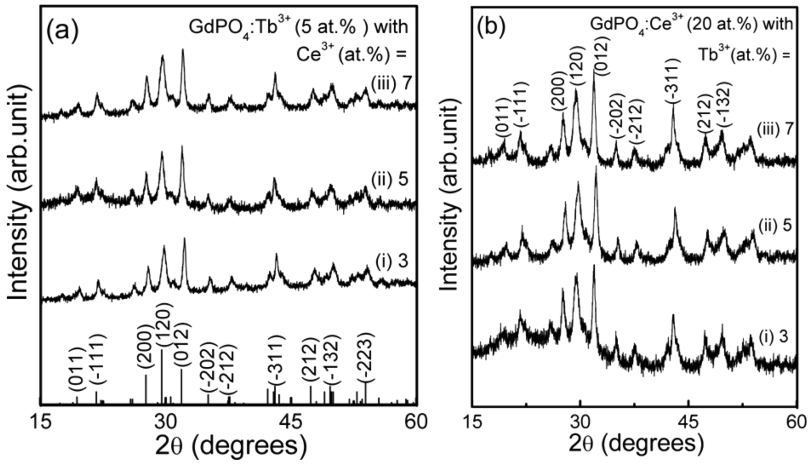

Figure 1. XRD patterns of as-synthesized $GdPO_4$ samples doped with (a) fixed 5 at. % Tb^{3+} and different Ce^{3+} at. % concentrations and (b) fixed 20 at. % Ce^{3+} and different Tb^{3+} at. % concentrations.

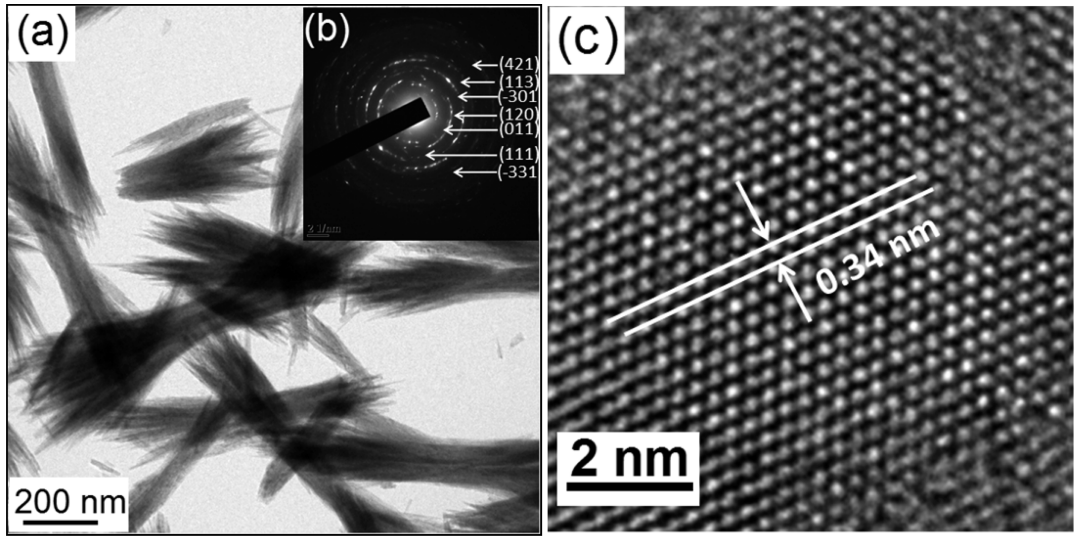

Figure 2. (a) TEM image of as-synthesized $GdPO_4$:Tb^{3+} (5 at. %)/Ce^{3+} (5 at. %) nanorods, (b) its SAED pattern, and (c) HRTEM image showing its lattice spacing.

the enhancement of Tb^{3+} emission.[34,35] Therefore it is important to study the energy transfer process and its dependence on the concentration of Ce^{3+} and Tb^{3+}. Based on the energy transfer from Ce^{3+} to Tb^{3+}, a luminescence switching mechanism is possible, which gathers attention for applications including chemical sensing.[36] In the process, the sequential quenching of green emission of $GdPO_4$:Tb^{3+}/Ce^{3+} in the presence of an oxidant (such as $KMnO_4$) occurs due to oxidation of Ce^{3+}→Ce^{4+}, leading to no energy transfer to Tb^{3+} (OFF state), and then luminescence can be recovered again by adding a reducing agent (ON state).

In addition, the Gd^{3+} ion has the highest seven unpaired electrons ($^8S_{7/2}$) in the 4f energy level with zero angular momentum under spin−orbit coupling. These electrons solely yield the S state electron magnetic moment. Thus, the Gd^{3+} ion can efficiently induce longitudinal relaxation of a water proton. So, the Gd^{3+} ion is known to be the best metal ion for a T_1 (longitudinal relaxation) contrast agent in magnetic resonance imaging (MRI). In view of this, there have been recent reports of Gd-chelates, $GdPO_4$, Gd_2O_3, $NaGdF_4$, etc., nanoparticles for an MRI contrast agent, which is a powerful and noninvasive medical diagnostic technique.[10,37−39]

In this investigation, photoluminescence (PL) studies of $GdPO_4$:Tb^{3+}/Ce^{3+} have been undertaken to confirm the occurrence of efficient energy transfer from Ce^{3+} to Tb^{3+}. We also have investigated the energy transfer process and its efficiency with the variation of Ce^{3+} and Tb^{3+} with steady-state luminescence and decay lifetime. The luminescence switching behavior and its correlation with energy transfer efficiency have been investigated with respect to the concentration of Ce^{3+} and Tb^{3+} ions. We have also looked into quantum yield, its redispersible nature in polar solvents, the formation of films with a polymer matrix, and the magnetic behaviors.

RESULTS AND DISCUSSION

XRD, FTIR, and Microstructure Studies. The X-ray diffraction (XRD) patterns of as-synthesized $GdPO_4$ doped with different concentrations of Ce^{3+} and Tb^{3+} are shown in Figure 1. The patterns of as-synthesized samples unambiguously match with the monoclinic phase of $GdPO_4$ (JCPDS-32-0386). Similar patterns in all the samples indicate the homogeneous solid solution among $GdPO_4$, $TbPO_4$, and $CePO_4$. This is due to the similar ionic radii of Gd^{3+} (1.107 Å), Tb^{3+} (1.095 Å), and Ce^{3+} (1. 196 Å) in a nine-coordination

dx.doi.org/10.1021/ph4001718 | ACS Photonics 2014, 1, 337−346

system,[40] which makes $GdPO_4$ a suitable matrix for incorporation of lanthanide ions. Not much difference in intensities is observed at 2θ (deg) = 29.51 and 31.89 because of the multiplicity of the planes (120) and (012) in the monoclinic structure.[19] The asymmetry in intensities observed between the most intense peaks may be ascribed to the anisotropic growth of the $GdPO_4$ nanoparticles in the rod shape (seen in the TEM image).

The Fourier transform infrared (FTIR) spectrum of 5 at. % Tb^{3+}-doped $GdPO_4$ nanoparticles is shown in Figure S1 (Supporting Information). Prominent bands are observed at 551, 569, 625, 881, 996, 1008, 1083, 1438, 1654, 2881, 2953, and 3321 cm^{-1}. Based on the $(PO_4)^{3-}$ group symmetry, band regions are defined as ν_1, ν_2, ν_3, and ν_4 respectively.[19] The band regions ν_1 and ν_2 are Raman-active modes, whereas ν_3 and ν_4 are IR-active modes and correspond to the stretching and bending vibrations of the $(PO_4)^{3-}$ group. The ν_4 region can be assigned at 551, 569, and 625 cm^{-1} and ν_3 at 881, 996, 1008, and 1083 cm^{-1}. Bands at 1654 and 3382 cm^{-1} correspond to bending and stretching vibrations of the O−H group of the ethylene glycol (EG) molecule.[41] The broad band at 3382 cm^{-1} is different from the free O−H stretching frequency (3650 cm^{-1}), indicating the presence of a hydrogen bond in EG molecules. The wagging vibration at 1266 cm^{-1}, twisting vibration at 1155 cm^{-1}, and rocking vibration at 899 cm^{-1} due to the presence of CH_2 from EG have been merged with the vibrational bands of $(PO_4)^{3-}$.[19] The peaks at 2881 and 2953 cm^{-1} correspond to the stretching vibrations of the CH_2 group from EG.[41]

The field emission scanning electron microscopy (FESEM) image of the $GdPO_4$:Tb^{3+} (5 at. %)/Ce^{3+} (5 at. %) nanorods is shown in Figure S2a (Supporting Information). The image clearly shows the bundle of nanorods of approximately 15−20 nm in diameter and 600−700 nm in length. Further the self-assembly of these nanorods was observed in the transmission electron microscopy (TEM) image shown in Figure 2a. The individual nanorods appear to be assembled forming broom-like nanostructures. The presence of Ce, Tb, Gd, and P is confirmed from energy-dispersive analysis of X-rays (EDAX) (Figure S2b in the Supporting Information). Figure 2b shows the selected area electron diffraction (SAED) pattern. The pattern shows that the samples are in the crystalline form. The calculated d-spacing of 0.30 nm from the high resolution TEM image (Figure 2c) can be matched with the plane (120) of $GdPO_4$.

Magnetic Study. The magnetization (M) versus applied magnetic field (H) plots of undoped and Tb^{3+}/Ce^{3+}-doped $GdPO_4$ nanorods are shown in Figure S3 (Supporting Information). All the samples show purely paramagnetic behavior, with a high paramagnetic moment due to possession of a higher number of unpaired electrons (7) in the half-filled $4f^7$ outermost orbital of the Gd^{3+} ion. The zero field cooling (ZFC) and field cooling (FC) measurements of undoped and 5 at. % Tb^{3+}-doped $GdPO_4$ nanoparticles at 500 Oe in the range of 330 to 5 K (Figures S4 and S5 in the Supporting Information) show typical Curie behavior with high moment, reaffirming the paramagnetic behavior. Thus, these lumino-magnetic nanoparticles with both luminescence and magnetic properties will be a potential multifunctional candidate for simultaneous applications in bioimaging and MRI.[10,16,34] The paramagnetic contribution coming from the half-filled $4f^7$ of the Gd^{3+} ion is calculated from the Curie equation,[42]

$$\mu = \sqrt{\frac{3k_B CA}{N_A}} \quad (1)$$

where k_B is the Boltzmann constant, C is the Curie constant, A is the atomic or molecular weight, and N_A is Avogadro's number. The estimated moment (in terms of Bohr magneton, μ_B) associated per atom of Gd^{3+} is found to be 5.9 μ_B, which is ∼75% of the theoretical value (7.9 μ_B). Here, the orbital contribution is neglected.

Photoluminescence (PL) Study. Excitation spectra of 5 at. % Tb^{3+}-doped $GdPO_4$ sensitized with different Ce^{3+} (3, 5, and 7 at. %) concentrations monitored at 544 nm emission are shown in Figure S6 (Supporting Information). The excitation spectra consist of three main absorption peaks at 250, 280, and 315 nm in the range of 200 to 320 nm. The first and second peaks are associated with the spin-allowed 4f−5d transitions in Ce^{3+} from the $^2F_{5/2}$ ground state of 4f to two different excited state levels of 5d, whereas the third one is related to the 4f−4f transition of Ce^{3+}.[35,43] The excitation peaks observed at $^7F_6 \rightarrow {}^5G_5$ (355 nm), $^7F_6 \rightarrow {}^5L_{10}$ (373 nm), and $^7F_6 \rightarrow {}^5G_6$ (380 nm) are related to the f−f transition absorptions of Tb^{3+} (inset of Figure S6).[35] The presence of a peak arising from the $^8S_{7/2} \rightarrow {}^6I_{11/2}$ transition of the Gd^{3+} ion at ∼278 nm is not observed separately because it is merged with spin-allowed 4f−5d transitions in Ce^{3+}. The presence of such strong absorption compared to the f−f transitions, which are of spin-forbidden nature, indicates the occurrence of strong energy transfer from Ce^{3+}/Gd^{3+} to the excited energy states of Tb^{3+} (discussed later).

PL emission spectra of $GdPO_4$:Tb^{3+} (5 at. %)/Ce^{3+} (5 at. %) under excitation at 250, 280, and 355 nm (Figure S7 in the Supporting Information) show the emission bands at 490 ($^5D_4 \rightarrow {}^7F_6$), 544 ($^5D_4 \rightarrow {}^7F_5$), 585 ($^5D_4 \rightarrow {}^7F_4$), and 620 ($^5D_4 \rightarrow {}^7F_3$) nm.[35] Among these, the green emission at 544 nm is the strongest. The broad emission observed at 350 nm after excitation with 250 and 280 nm is due to radiative transitions from the d-level excited states of Ce^{3+} to its f-level ground states. The emission intensity area excited at 280 nm is nearly 15 times more compared to that at 355 nm excitation under similar conditions. This shows the strong energy transfer from the Ce^{3+} ions' absorption to the excited states of Tb^{3+} ions. This is clearly evident from the overlapping of the broad Ce^{3+} emission with f−f absorption bands of Tb^{3+} (see Figure S8 in the Supporting Information). It is well known that according to Föster−Dexter energy transfer theory, the transfer of energy between two fluorophors occurs if these are within a critical distance (∼20 Å) and the donor's emission and the acceptor's absorption bands overlap.[44,45] The schematic representation of energy transfer taking place in $GdPO_4$:Tb^{3+}/Ce^{3+} is shown in Figure S9 (Supporting Information). To investigate the effect of Ce^{3+} concentration, emissions of $GdPO_4$:Tb^{3+} (5 at. %) sensitized with different Ce^{3+} concentrations excited at 280 nm are shown in Figure 3. It is observed that the intensity of Tb^{3+} emission increases with the increase of Ce^{3+} concentration up to 7 at. % and then decreases. The decrease in the Tb^{3+} emission with the increase of Ce^{3+} concentration (above 7 at. %) might be due to the following reasons. There may be critical concentrations of Ce^{3+} with respect to Gd^{3+} for a particular host (here it is $GdPO_4$), where the absorption cross-section near 250−290 nm (absorption level of Ce^{3+}/Gd^{3+}) will be maximum. In this, there is a high probability of energy transfer to Tb^{3+}. When the amount of Ce^{3+} increases, simultaneously

dx.doi.org/10.1021/ph4001718 | ACS Photonics 2014, 1, 337−346

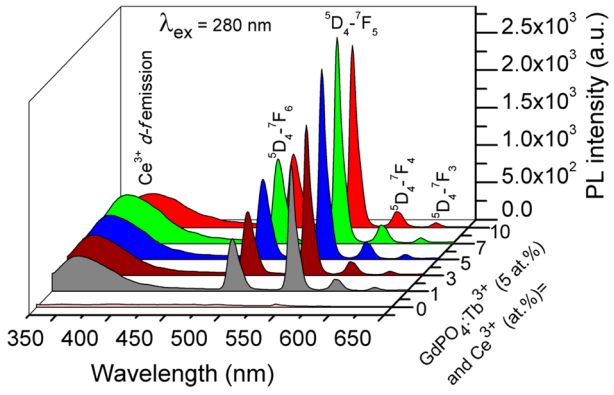

Figure 3. Emission spectra of $GdPO_4$:Tb^{3+} (5 at. %) sensitized with different Ce^{3+} concentrations excited at 280 nm.

the amount of Gd^{3+} decreases in the system ($Gd_{1-x-y}Ce_xTb_{y=0.05}PO_4$). Thus, there will be net effect from Ce^{3+} and Gd^{3+} in the absorption as well as emission processes. At 10 at. % Ce^{3+}, a decrease in emission intensity of Ce^{3+}/Tb^{3+} may be due to the net effect from Ce^{3+}/Gd^{3+} or dipole−quadrupole interactions among the Ce^{3+} ions.

To further explore the energy transfer processes and their efficiency from the Ce^{3+} emission to the Tb^{3+} excited states, we have investigated the emissions of different Tb^{3+} concentrations sensitized with Ce^{3+} (20 at. %). 20 at. % Ce^{3+} has been chosen to accommodate higher concentration of Tb^{3+} ions in the host $GdPO_4$ for energy transfer study. Figure 4 shows the

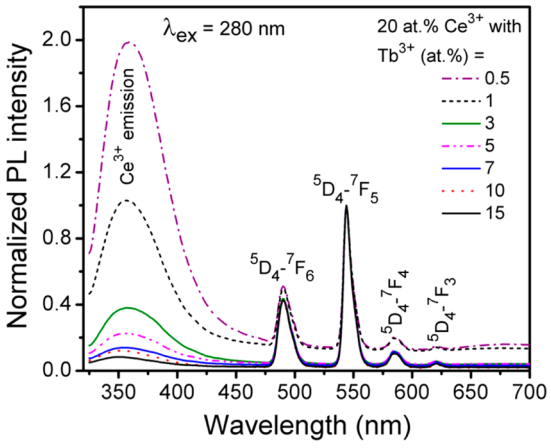

Figure 4. Normalized (at λ = 544 nm) emission spectra of Ce^{3+}-sensitized $GdPO_4$:Tb^{3+} (5 at. %) samples under 280 nm excitation.

normalized (at λ = 544 nm) emission spectra of Ce^{3+}-sensitized $GdPO_4$:Tb^{3+} samples after excitation at 280 nm. From the spectra, it is clearly evident that the intensity of the broad emission peak of the Ce^{3+} ions (320 to 420 nm) gradually decreases with an increase in the Tb^{3+} concentration. This gradual decrease in Ce^{3+} emission intensity indicates an increase in energy transfer efficiency with the increase in Tb^{3+} concentration. This happens because electrons from Ce^{3+} emission find more and more Tb^{3+} ions in the system for resonance-type energy transfer.

PL Decay and Quantum Yield Studies. Figure 5 shows the PL decay of the 20 at. % Ce^{3+}-sensitized $GdPO_4$:Tb^{3+} samples with monitoring emission at 544 nm and excitation at 280 nm. In this case, the excitation of Tb^{3+} occurs through

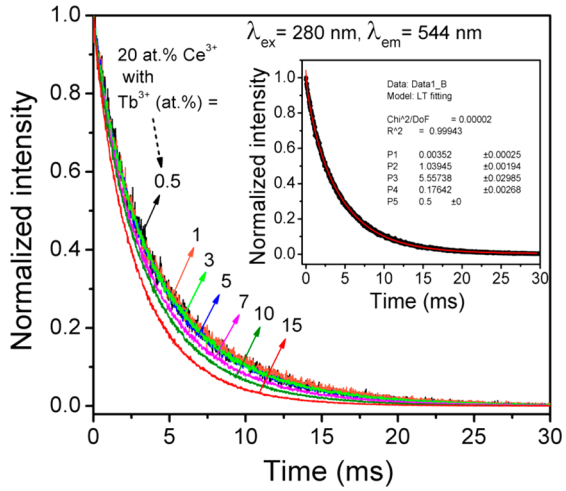

Figure 5. Luminescence decay of the 20 at. % Ce^{3+} and different Tb^{3+} concentrations doped $GdPO_4$ samples (λ_{ex} = 280 nm and λ_{em} = 544 nm). Inset: Typical fitting of $GdPO_4$:Tb^{3+}/Ce^{3+} (both are 5 at. %) nanorod.

resonance energy transfer from Ce^{3+} emission to Tb^{3+}. Thus the decay does not occur immediately after excitation. In such cases, the decay process follows the form[45]

$$I(t) = I_0 \exp[(-t/\tau) - (2bt^{1/2})] \quad (2)$$

where b is quencher concentration and is diffusion coefficient dependent. Assuming resonance energy transfer occurs in three dimensions, t has the powers of 1/2. On the basis of the above equation, the luminescence decay times of Tb^{3+} in 20 at. % Ce^{3+}-sensitized $GdPO_4$:Tb^{3+} have been calculated and are presented in Table 1. The inset of Figure 5 shows the typical

Table 1. Decay Lifetime Values of Tb^{3+} and Ce^{3+} in Different Tb^{3+} Concentrations and Fixed 20 at. % Ce^{3+}-Doped $GdPO_4$

		lifetime τ and goodness of fit R^2			
sl. no.	Tb^{3+} (at. %)	Tb^{3+} (ms)	R^2	Ce^{3+} (ns)	R^2
1	0.5	6.6	0.99	10	0.99
2	1	6.8	0.99	9	0.98
3	3	5.6	0.99	8	0.98
4	5	5.7	0.99	8	0.98
5	7	5.1	0.99	6	0.98
6	10	4.5	0.99	5	0.98
7	15	3.7	0.99	4	0.98

fitting of Tb^{3+} decay in $GdPO_4$:Tb^{3+} (5 at. %)/Ce^{3+} (5 at. %) sample. The maximum lifetime (6.8 ms) of Tb^{3+} is found at $GdPO_4$:Tb^{3+} (1 at. %)/Ce^{3+} (20 at. %), which is comparatively longer than earlier reported,[46] which might be due to a decrease in nonradiative transition probabilities. The lifetime value decreases with an increase in concentration. This is ascribed to the increase in contribution of nonradiative transition probabilities as the lifetime depends on $(k_r + k_{nr})^{-1}$, where k_r and k_{nr} are the respective radiative and nonradiative transition probabilities. The increase in k_{nr} is due to concentration quenching, which is a typical property of lanthanide ions. Figure 6 shows the PL decay curve of Ce^{3+} emission (355 nm) excited at 280 nm. The lifetime value of Ce^{3+} in $GdPO_4$:Tb^{3+}/Ce^{3+} is found to be in the range of 4−10 ns, which is much shorter than the Ce^{3+} lifetime (10−150 ns) in $Ca_2Al_3O_6F$:Ce^{3+}/Tb^{3+} reported by Xia et al.[47] The lifetime of 20 at. % Ce^{3+}-

dx.doi.org/10.1021/ph4001718 | ACS Photonics 2014, 1, 337−346

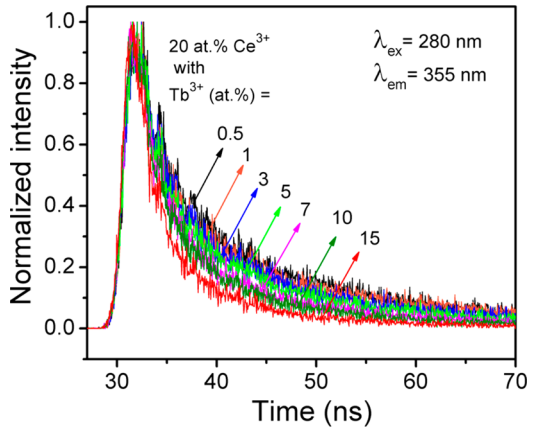

Figure 6. Luminescence decay of Ce^{3+} emission in 20 at. % Ce^{3+} and different Tb^{3+} concentrations doped $GdPO_4$ samples (λ_{ex} = 280 nm and λ_{em} = 355 nm).

doped $GdPO_4$ without any Tb^{3+} was found to be 50 ns (Figure S10 in the Supporting Information). The shorter lifetime is an indication of nonradiative energy transfer from Ce^{3+} emission to excited states of Tb^{3+}. From Table 1, it is clearly observed that the lifetime decreases with an increase in Tb^{3+} concentration. This is due to the increase in nonradiative resonance energy transfer to the higher excited states of Tb^{3+} (mentioned earlier). This confirms the increase in the energy transfer efficiency with the increase in Tb^{3+} ions in the system. The quantum yield of $GdPO_4$:Tb^{3+}(5 at. %)/Ce^{3+}(7 at. %), henceforth termed $Gd_{0.88}Ce_{0.07}Tb_{0.05}PO_4$, dispersed in water was measured using a $BaSO_4$-coated integrated sphere, and it is found to be 28%.

CIE, Redispersion, and Polymer Film Formation. For the understanding of color tone of the light emission from the samples, the color coordinates (x, y) are given in a CIE chromaticity diagram (labeled with numericals) in Figure 7. The details of the coordinates are presented in Table S1 (Supporting Information). From the coordinates, it is observed

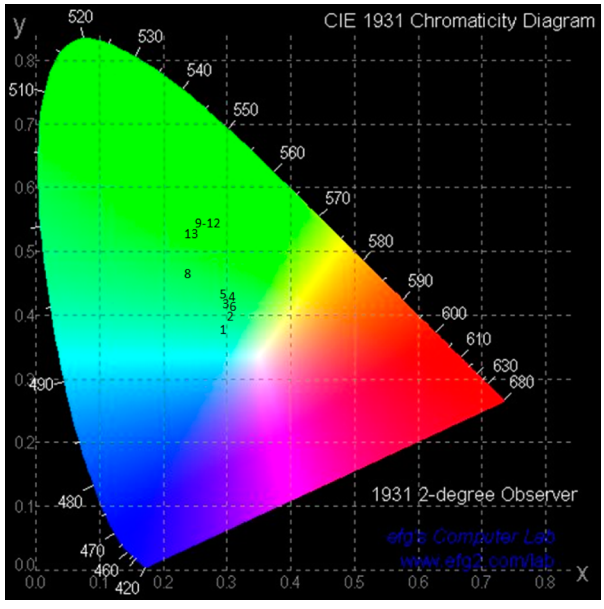

Figure 7. CIE color coordinates (x, y numbered with numericals) in CIE chromaticity diagram (1993).

that the color of the samples is tuned from greenish-blue to proper green. The emission colors of the samples are moved toward greenish-blue if the Tb^{3+} concentration decreases in $GdPO_4$:Ce^{3+} (20 at. %)-doped samples. The presence of greenish-blue emission is understandable, as the violet-blue color originating from Ce^{3+} emission is mixed with green color from Tb^{3+}.

As-prepared samples are redispersible in polar solvents such as ethanol, methanol, and water. Redispersion is due to the presence of an O−H group adsorbed/bonded on the surface of the particles, which comes from the capping agent ethylene glycol. EG simultaneously plays the role of solvent and capping agent. The O−H group of EG can form a hydrogen bond with polar solvents. The presence of an O−H group on the surface of the particles was confirmed in the FTIR study. Further, about 5 mg of particles is dispersed in 5 mL of water and mixed with 10 mL of 4 wt.% polyvinyl alcohol (PVA) solution. After thoroughly mixing in an ultrasonic bath, the mixture was treated with 1 mL of a 0.1 M solution of borax, which helps in cross-linking between PVA molecules. Then the polymer composite film was prepared by spreading the above viscous solution over the glass slide, and a film with a thickness of ∼1 mm is formed after drying. Both the dispersed sample and polymer film show strong green emission with UV light irradiation (280 nm), which is shown in Figure 8. More efficient light emission is also evident for Ce^{3+}-sensitized $GdPO_4$:Tb^{3+}, as the green color is more intense (Figure 8b) than that for $GdPO_4$:Tb^{3+} (Figure 8a). Such dispersed samples may be useful for tagging with bioentities in imaging. Also, such polymer-based films will pave a new dimension toward development of flexible light-emitting display devices.

Luminescence Switching. A luminescence ON−OFF study of $Gd_{0.88}Ce_{0.07}Tb_{0.05}PO_4$ nanorods was done by subsequent addition of oxidizing agent (potassium permanganate, $KMnO_4$) and reducing agent (ascorbic acid, $C_6H_8O_6$) and is shown in Figure 9. Based on the following equations,

$$3Ce^{3+} + MnO_4^- + 2H_2O \rightarrow 3Ce^{4+} + MnO_2 + 4OH^- \quad (3)$$

$$2Ce^{4+} + C_6H_8O_6 \rightarrow 2Ce^{3+} + C_6H_6O_6 + 2H^+ \quad (4)$$

one MnO_4^- ion can oxidize three Ce^{3+} ions, whereas one $C_6H_8O_6$ can reduce two Ce^{4+} ions. At the initial stage, 20 mg of $Gd_{0.88}Ce_{0.07}Tb_{0.05}PO_4$ was dispersed in 1 mL of EG, and this contains ∼3.4 × 10^{19} Ce^{3+} ions. These Ce^{3+} ions can be completely oxidized to Ce^{4+} with the addition 0.3 mg of $KMnO_4$. The charge transfer from Ce^{3+} to Ce^{4+} occurs; thereby energy transfer from Ce^{3+} to Tb^{3+} is cut off when excited through Ce^{3+} (278 nm, i.e., allowed transition from $4f^1$ to $5d^0$ transition). The Ce^{4+} state is a full cell ion having the electronic configuration $[Xe]4f^05d^06s^0$. Hence, no 4f−4f electronic transitions can occur because of the empty 4f level. Eventually, no emission from Tb^{3+} should occur. But, the coexistence of Ce^{3+} with Ce^{4+} cannot be ignored, which is the case more often than not. Again, the luminescence can be restored by addition of ascorbic acid (0.35 mg) because of the reduction process from Ce^{4+} to Ce^{3+}. This process is like the ON−OFF cycle. It can be repeated five times. However, the emission intensity decreases with the number of cycles due to the decrease of active ions (Ce^{3+} and Tb^{3+}) per 1 mL of the system and also the extent of increase of quenchers arises from $KMnO_4$, MnO_2, or $C_6H_8O_6$. Thus, this system can be used as a luminescence switch through redox reaction. Further, this has been confirmed

dx.doi.org/10.1021/ph4001718 | ACS Photonics 2014, 1, 337−346

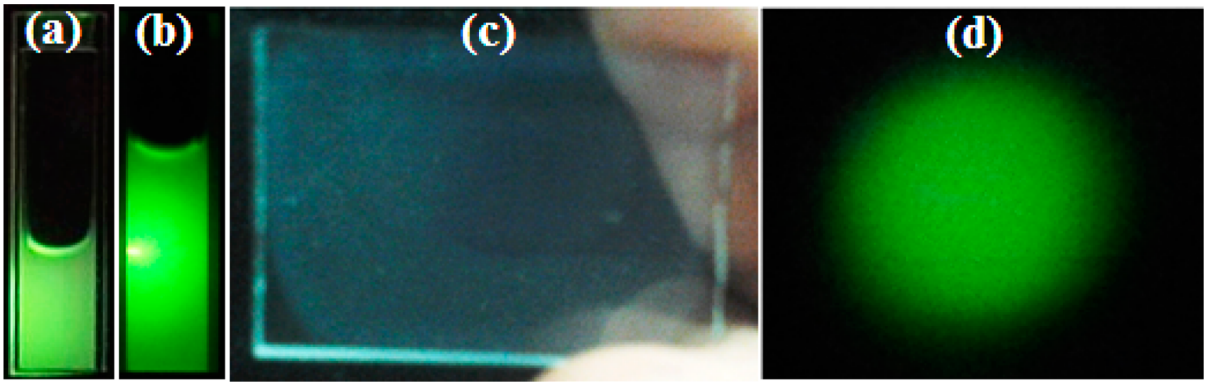

Figure 8. Photographs: (a) $GdPO_4:Tb^{3+}$ (5 at. %) and (b) $GdPO_4:Tb^{3+}$ (5 at. %)/Ce^{3+} (7 at. %) dispersed in water under UV excitation; PVA polymer thin films (c) without and (d) with UV excitation.

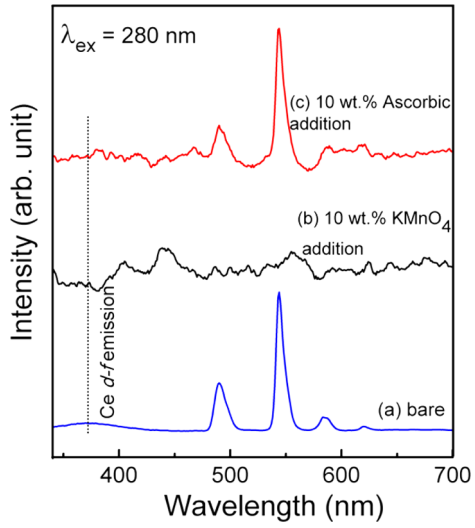

Figure 9. PL emission of (a) bare, (b) oxidized with $KMnO_4$, and (c) reduced with ascorbic acid 7 at. % Ce^{3+}-sensitized $GdPO_4:Tb^{3+}$ (5 at. %).

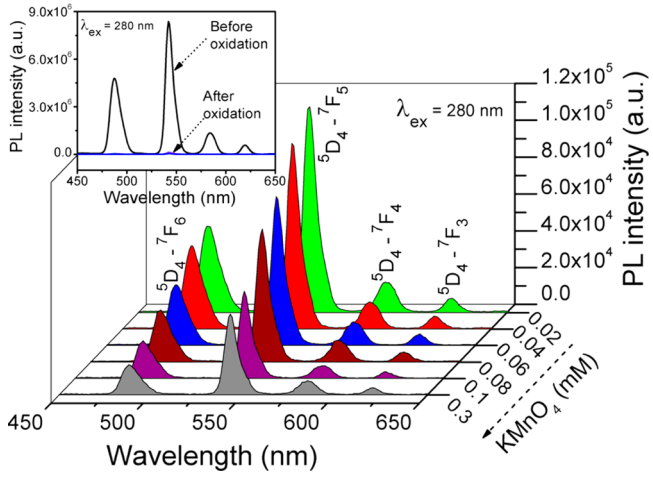

Figure 10. PL emission spectra (λ_{ex} = 280 nm) of $Gd_{0.88}Ce_{0.07}Tb_{0.05}PO_4$ after oxidizing with $KMnO_4$ solution (0.02–0.3 mM). The treatment time was kept fixed for 2 h. Inset: Comparison of PL emission spectra of the sample before and after oxidation treatment.

with the quantum yield measurement with three cycles of ON/OFF. The respective quantum yields after first, second, and third cycles (1 cycle = one OFF to ON state) are found to be 22%, 18%, and 10%, respectively.

The second protocol for the switching behavior was carried out using water as the medium for dispersion. The detailed study is given in the Supporting Information. After the alternate addition of $KMnO_4$ and ascorbic acid, the precipitate was removed by centrifugation followed by washing. Here, the powders obtained from the precipitate were recorded for luminescence. This reduces the effect from the extra byproducts ($KMnO_4$, MnO_2, K^+, $C_6H_8O_6$, $C_6H_6O_6$, etc.) coming out during the experiment, and these byproducts are a source of quencher in the luminescence observed in the first protocol.

Figure 10 shows PL emission spectra of the $Gd_{0.88}Ce_{0.07}Tb_{0.05}PO_4$ nanorods after it was given a partial oxidizing treatment by the $KMnO_4$ solution with varying concentrations between 0.02 and 0.3 mM. The excitation wavelength (λ_{ex}) is fixed at 280 nm. The treatment time was kept fixed at 2 h. It has been observed that with increasing the concentration of $KMnO_4$, the PL intensity gradually decreases due to an increase in the oxidation rate and more Ce^{3+} ions are converted to Ce^{4+}, resulting in the lowering of energy transfer from Ce^{3+} to Tb^{3+}. This is also confirmed from the significant decrease in the intensity of Ce^{3+} (d–f) emission (Figure S11a in the Supporting Information). In addition, a slight blue shift is observed in the emission peak (the strongest one, i.e., $^5D_4$–$^7F_5$). This may be due to the change in the stoichiometry after the formation of Ce^{4+}. It has been observed even at a higher concentration of $KMnO_4$ (0.3 mM) that the luminescence is not quenched completely. This is indicated by all Ce^{3+} ions not being converted to Ce^{4+}. Hence it is more likely to be a surface phenomenon.[48] However, the luminescence is almost quenched in the oxidized sample in comparison to the unoxidized one (inset of Figure 10). In our opinion, there are surface and core/lattice Ce^{3+} ions in a particle. When a sufficient amount of $KMnO_4$ solution is added to particles in order to convert all Ce^{3+} to Ce^{4+} ions, the system can be taken as heterogeneous (i.e., particles/solid + solution). The following may be expected: (1) oxidation from Ce^{3+} present on the surface of the particle to Ce^{4+} occurs at an initial stage and (2) oxidation of Ce^{3+} in the lattice/core to Ce^{4+} occurs after a longer duration. However, we observed that there are still emission peaks corresponding to Tb^{3+} after the oxidation reaction, but their intensity is significantly decreased as compared to unoxdized ones. This means that most Ce^{3+} ions are converted to Ce^{4+} ions and some Ce^{3+} ions are still remain in the core/lattice.

dx.doi.org/10.1021/ph4001718 | ACS Photonics 2014, 1, 337–346

Figure 11 shows the PL emission spectra of a heavily oxidized $Gd_{0.88}Ce_{0.07}Tb_{0.05}PO_4$ sample (0.1 mM $KMnO_4$) after

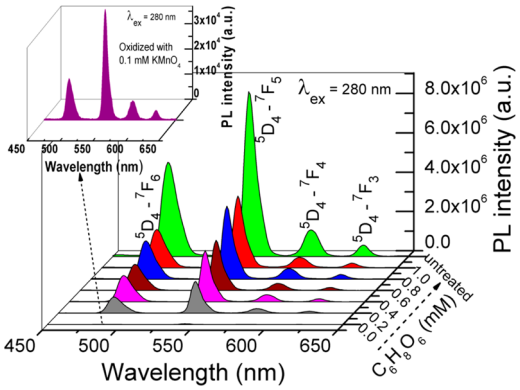

Figure 11. PL emission spectra (λ_{ex} = 280 nm) of heavily oxidized $Gd_{0.88}Ce_{0.07}Tb_{0.05}PO_4$ (oxidized with 0.1 mM $KMnO_4$) after reducing with ascorbic acid solution (0−1 mM). A PL emission spectrum of untreated sample is included for comparison. Inset: Magnified graph of a selected plot marked with an arrow. The treatment time was kept fixed at 2 h.

partial reduction by ascorbic acid solution at different concentrations between 0 and 1 mM. A PL emission spectrum of untreated/unoxidized sample is included for comparison. It has been observed that luminescence is recovered with the increase in concentration of $C_6H_8O_6$ from 0.2 mM to 1 mM, resulting in the gradual increase of luminescent intensity. This is due to the reverse effect of the oxidation, resulting in the recovery of the Ce^{3+} state from the Ce^{4+} state, which is reflected in the Ce^{3+} (d−f) emission (Figure S11b in the Supporting Information). Here also, complete recovery is not observed as that of the untreated sample because complete reduction is not possible. This is related to surface phenomena. Another possibility arises from the quenchers, such as $KMnO_4$, $C_6H_8O_6$, or OH, associated during the reaction, which might not be removed from the sample completely.

Figure 12 shows the emission spectra of the sample after repeated cycles of switching for five cycles. Oxidation (X) is followed by reduction (R) in the sequence X1-R1-X2-R2-X3-R3-X4-R4-X5-R5. The concentration of the oxidant and reductant were 0.1 and 1.0 mM, respectively. The duration of oxidation or reduction is kept fixed at 10 min each, followed by a centrifugation time of 5 min after each cycle. It is observed that the luminescence intensity decreases gradually in the oxidation cycle, while the recovery in the reduction cycle is prominent up to the second cycle, followed by a decrease. The recovery is substantial up to the fifth cycle of the experiment.

The time response of the luminescence switching was evaluated for the sample in the oxidation treatment with the $KMnO_4$ solutions (0.02−0.1 mM). The plot of integrated PL intensity versus time is shown in Figure 13. The integrated PL

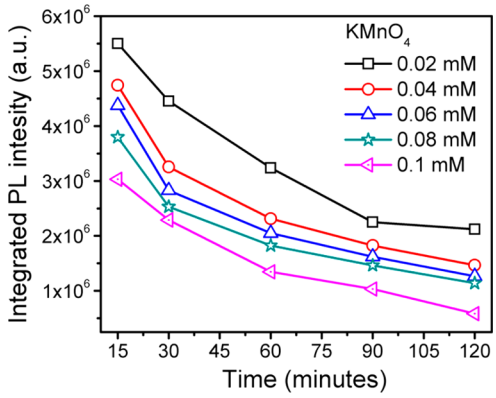

Figure 13. Time dependence of the integrated PL intensity for the oxidized sample with $KMnO_4$ solution with varying concentrations between 0.02 and 0.1 mM. The integrated PL intensity was calculated as the area between 450 and 650 nm in the emission spectra (λ_{ex} = 280 nm).

intensity for the Tb^{3+} emissions was calculated by estimating the area under the emission spectra (λ_{ex} = 280 nm) between wavelengths of 450 and 650 nm. Gradual luminescence quenching is observed with time for all of the concentrations. However, complete quenching is not observed in any case even at higher concentrations of $KMnO_4$. This oxidation reaction takes place predominantly at the surface of the particles.

CONCLUSIONS

Enhanced luminescence of Ce^{3+}-sensitized $GdPO_4$ nanorods activated with Tb^{3+} was successfully investigated for the energy transfer mechanism. Efficient energy transfer is observed up to 20 at. % Ce^{3+} content without noticeable cross relaxation among them. The nanorods are readily redispersible in polar solvents. They could be easily incorporated in polymer-based films for promising flexible display devices. The extent of luminescence switching in Ce^{3+}-sensitized $GdPO_4$:Tb^{3+}, which

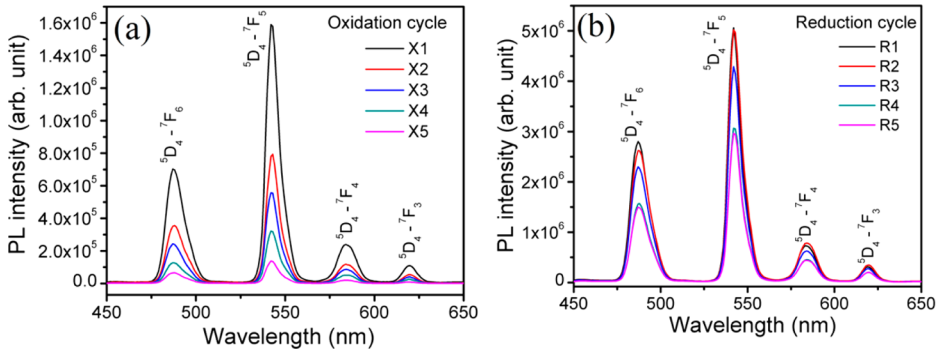

Figure 12. PL emission spectra (λ_{ex} = 280 nm) of $Gd_{0.88}Ce_{0.07}Tb_{0.05}PO_4$ after repeated switching for five cycles. Oxidation (X) is followed by reduction (R) in the sequence X1-R1-X2-R2-X3-R3-X4-R4-X5-R5. The concentration of the oxidant and reductant were 0.1 and 1.0 mM, respectively. The duration of oxidation and reduction is 10 min each, followed by centrifugation for 5 min after each cycle.

dx.doi.org/10.1021/ph4001718 | ACS Photonics 2014, 1, 337−346

occurs due to conversion of Ce^{3+} to Ce^{4+} and vice versa, depends on the concentration of oxidizing agent ($KMnO_4$) and reducing agent (ascorbic acid) as well as on the times scale. The optical switching in $GdPO_4:Ce^{3+}/Tb^{3+}$ is more likely to be a surface phenomenon. The luminescence quantum yield for $Gd_{0.88}Ce_{0.07}Tb_{0.05}PO_4$ is found to be 28%. Tb^{3+}/Ce^{3+}-doped $GdPO_4$ samples are highly paramagnetic and show a strong luminescent property, which could be potentially useful for simultaneous optical and MR imaging.

EXPERIMENTAL SECTION

Synthesis of Ce^{3+}-Sensitized $GdPO_4:Tb^{3+}$ Nanorods. Analytical grade reagents were used as reactants without further purification. Gd_2O_3 (Aldrich, 99.99%), $Tb(NO_3)_3{\cdot}6H_2O$ (Alfa Aesar, 99.99%), $Ce(NO_3)_3{\cdot}6H_2O$ (Aldrich, 99.99%), and $NH_4H_2PO_4$ (Aldrich, 99.999%) were used as precursors. EG and hydrochloric acid (HCl) were used as received. For the synthesis of $GdPO_4:Tb^{3+}/Ce^{3+}$, a simple polyol method using EG was adopted following earlier reports.[19] In a typical synthesis procedure for $GdPO_4:Tb^{3+}$ (5 at. %)/ Ce^{3+} (5 at. %) nanorods, 350 mg of Gd_2O_3, 49 mg of $Tb(NO_3)_3{\cdot}6H_2O$, and 47 mg of $Ce(NO_3)_3{\cdot}6H_2O$ were dissolved in 1 mL of 1 M HCl in a 100 mL round-bottom flask. The excess acid was removed by evaporating the solution through successive addition of water (5 mL). Then 250 mg of $(NH_4)H_2PO_4$ was added to the resulting transparent solution along with 50 mL of EG. The solution was heated at 150 °C for 2 h. The resulting white precipitates were washed with a mixture of water and ethanol and collected by centrifugation. The chemical equation for the formation of $LnPO_4$ (Ln = Gd, Eu, Ce) is

$$Ln^{3+} + 3Cl^- + 3(NH_4)H_2PO_4 + xH_2O \rightarrow LnPO_4{\cdot}xH_2O \downarrow + 3NH_4Cl + 2H_3PO_4 \ (x = 0-3)$$

Characterization Techniques. The identification and purity of the phase was confirmed by XRD using a PANalytical diffractometer (X'pert PRO) with Cu Kα radiation (λ = 1.5405 Å) and a Ni filter. FTIR spectra were recorded in Magna550, Nicolet Instruments Corporation, USA, by KBr pellet technique. FESEM and TEM images were recorded in JEOL JEM-7600F and JEOL JEM-2100F instruments, respectively. Magnetic measurements were carried out in a magnetic properties measurement system (MPMS, Quantum Design, USA).

The luminescence spectra were recorded at room temperature with a Hitachi F-4500 fluorescence spectrometer having a 150 W Xe lamp as the excitation source. Luminescence lifetime measurements for Tb^{3+} and Ce^{3+} transitions were carried out using a 100 W μs flash and nanosecond lamp attached to an Edinburgh Instruments (FLS920) apparatus equipped with a 450 W xenon arc lamp having a Peltier element cooled red-sensitive Hamamatsu R955 PMT. Instrumental response function was recorded using Teflon after excitation at 280 nm, and its lifetime is found to be less than 1 ns. For steady state PL measurement, a 50 mg amount of the powder sample was mixed with 1 mL of methanol and pasted over the quartz slide (1 cm × 1 cm) and dried in the ambient condition. All fittings to the decay data were carried out above 55−100 μs due to a delay in time response. For PL decay measurement, a 5 mg amount of the particles was dispersed in 200 μL of methanol and pasted over the quartz slide. Then it was dried at room temperature and put in the sample holder of the instrument. Excitation and emission of Tb^{3+} were monitored at 280 and 545 nm. Similarly, for Ce^{3+}, the monitoring excitation and emission were at 280 and 355 nm, respectively. The PL spectra of the luminescence switching experiment were recorded in a Horiba Jobin-Yvon Spex Fluorolog-3 fluorimeter. Quantum yields of the samples were measured using a $BaSO_4$-coated integrating sphere of diameter 15 cm in FLS920, which is based on the absolute method. For quantum yield measurement, a 1 mg amount of the as-prepared sample was dispersed in 1 mL of water. Excitation at 280 nm and emission at 544 nm were fixed. The slit widths for excitation and emission were fixed at 3 and 0.7 nm, respectively. The iris was kept at 90%. The data were recorded with a step size of 0.1 nm and dwell time of 0.3 s. The instrument was calibrated using rhodamine B standard dye with a quantum yield of 31% in water.[49]

ASSOCIATED CONTENT

Supporting Information

FTIR spectrum, FESEM image, EDX spectrum, $M-H$ plot, ZFC-FC plot, PL emission and excitation spectra, scheme for energy transfer process in $GdPO_4:Tb^{3+}/Ce^{3+}$, luminescence decay, CIE coordinates, and protocol for redox experiment. This material is available free of charge via the Internet at http://pubs.acs.org.

AUTHOR INFORMATION

Corresponding Authors

*(R. S. Ningthoujam) E-mail: rsn@barc.gov.in. Tel: +91 22 25592321. Fax: +91 22 25505151.

*(D. Bahadur) E-mail: dhirenb@iitb.ac.in. Tel: +91 22 25767632. Fax: +91 22 25763480.

Notes

The authors declare no competing financial interest.

ACKNOWLEDGMENTS

Financial support from the Nanomission of the Department of Science and Technology (DST), Government of India, is gratefully acknowledged. The authors are grateful to CRNTS, IIT Bombay, for TEM and SEM facilities. R. S. Ningthoujam thanks Mr. Amresh Prasad for extensive help.

REFERENCES

(1) Yan, R.; Gargas, D.; Yang, P. Nanowire photonics. *Nat. Photonics* **2009**, *3*, 569−576.

(2) Ariga, K.; Vinu, A.; Yamauchi, Y.; Ji, Q. M.; Hill, J. P. Nanoarchitectonics for mesoporous materials. *Bull. Chem. Soc. Jpn.* **2012**, *85*, 1−32.

(3) Zhu, M.; Nie, G.; Meng, H.; Xia, T.; Nel, A.; Zhao, Y. Physicochemical properties determine nanomaterial cellular uptake, transport, and fate. *Acc. Chem. Res.* **2013**, *46*, 622−631.

(4) Jariwala, D.; Sangwan, V. K.; Lauhon, L. J.; Marks, T. J.; Hersam, M. C. Carbon nanomaterials for electronics, optoelectronics, photovoltaics, and sensing. *Chem. Soc. Rev.* **2013**, *42*, 2824−2860.

(5) Kumar, S.; Daverey, A.; Sahu, N. K.; Bahadur, D. In vitro evaluation of PEGylated mesoporous $MgFe_2O_4$ magnetic nanoassemblies (MMNs) for chemo-thermal therapy. *J. Mater. Chem. B* **2013**, *1*, 3652−3660.

(6) Shields, A. J. Semiconductor quantum light sources. *Nat. Photonics* **2007**, *1*, 215−223.

(7) Jüstel, T.; Nikol, H.; Ronda, C. New developments in the field of luminescent materials for lighting and displays. *Angew. Chem., Int. Ed.* **1998**, *37*, 3085−3103.

(8) Gautam, A.; van Veggel, F. C. J. M. Blue electroluminescence from Eu^{2+}-doped GaN@SiO_2 nanostructures tuned to industrial standards. *Chem. Mater.* **2011**, *23*, 4817−4823.
(9) Singh, N. S.; Sahu, N. K.; Bahadur, D. Multicolor tuning and white light emission from lanthanide doped $YPVO_4$ nanorods: energy transfer studies. *J. Mater. Chem. C* **2014**, *2*, 548−555.
(10) Park, J. Y.; Baek, M. J.; Choi, E. S.; Woo, S.; Kim, J. H.; Kim, T. J.; Jung, J. C.; Chae, K. S.; Chang, Y.; Lee, G. H. Paramagnetic ultrasmall gadolinium oxide nanoparticles as advanced T_1 MRI contrast agent: account for large longitudinal relaxivity, optimal particle diameter, and *in vivo* T_1 MR images. *ACS Nano* **2009**, *3*, 3663−3669.
(11) Wang, G.; Peng, Q.; Li, Y. Lanthanide-doped nanocrystals: synthesis, optical-magnetic properties, and applications. *Acc. Chem. Res.* **2011**, *44*, 322−332.
(12) Escribano, P.; Julián-López, B.; Planelles-Aragó, J.; Cordoncillo, E.; Vian, B.; Sanchez, C. Photonic and nanobiophotonic properties of luminescent lanthanide-doped hybrid organic-inorganic materials. *J. Mater. Chem.* **2008**, *18*, 23−40.
(13) Xu, L.; Dong, B.; Wang, Y.; Bai, X.; Chen, J.; Liu, Q.; Song, H. Porous In_2O_3:RE (RE = Gd, Tb, Dy, Ho, Er, Tm, Yb) nanotubes: electrospinning preparation and room gas-sensing properties. *J. Phys. Chem. C* **2010**, *114*, 9089−9095.
(14) Zhang, F.; Wong, S. S. Ambient large-scale template-mediated synthesis of high-aspect ratio single-crystalline, chemically doped rare-earth phosphate nanowires for bioimaging. *ACS Nano* **2010**, *4*, 99−112.
(15) Petoral, R. M., Jr.; Söderlind, F.; Klasson, A.; Suska, A.; Fortin, M. A.; Abrikossova, N.; Selegård, L.; Käll, P.-O.; Engström, M.; Uvdal, K. Synthesis and characterization of Tb^{3+}-doped Gd_2O_3 nanocrystals: a bifunctional material with combined fluorescent labeling and MRI contrast agent properties. *J. Phys. Chem. C* **2009**, *113*, 6913−6920.
(16) Rodriguez-Liviano, S.; Becerro, A. I.; Alcántara, D.; Grazú, V.; de la Fuente, J. M.; Ocaña, M. Synthesis and properties of multifunctional tetragonal Eu:$GdPO_4$ nanocubes for optical and magnetic resonance imaging applications. *Inorg. Chem.* **2013**, *52*, 647−654.
(17) Singh, N. S.; Kulkarni, H.; Pradhan, L.; Bahadur, D. A multifunctional biphasic suspension of mesoporous silica encapsulated with YVO_4:Eu^{3+} and Fe_3O_4 nanoparticles: synergistic effect towards cancer therapy and imaging. *Nanotechnology* **2013**, *24*, 065101 (1−11).
(18) Wang, F.; Wang, J.; Liu, X. Direct evidence of a surface quenching effect on size-dependent luminescence of upconversion nanoparticles. *Angew. Chem., Int. Ed.* **2010**, *49*, 7456−7460.
(19) Sahu, N. K.; Ningthoujam, R. S.; Bahadur, D. Disappearance and recovery of luminescence in $GdPO_4$:Eu^{3+} nanorods: propose to water/OH^- release under near infrared and gamma irradiations. *J. Appl. Phys.* **2012**, *112*, 014306 (1−12).
(20) Boyer, J. C.; Manseau, M. P.; Murray, J. I.; van Veggel, F. C. J. M. Surface modification of upconverting NaYF4 nanoparticles with PEG-phosphate ligands for NIR (800 nm) biolabeling within the biological window. *Langmuir* **2010**, *26*, 1157−1164.
(21) Yin, A.; Zhang, Y.; Sun, L.; Yan, C. Colloidal synthesis and blue based multicolor upconversion emissions of size and composition controlled monodisperse hexagonal $NaYF_4$: Yb,Tm nanocrystals. *Nanoscale* **2010**, *2*, 953−959.
(22) Huignard, A.; Buissette, V.; Franville, A.-C.; Gacoin, T.; Boilot, J.-P. Emission processes in YVO_4:Eu nanoparticles. *J. Phys. Chem. B* **2003**, *107*, 6754−6759.
(23) Bai, X.; Song, H.; Pan, G.; Liu, Z.; Lu, S.; Di, W.; Ren, X.; Lei, Y.; Dai, Q.; Fan, L. Luminescent enhancement in europium-doped yttria nanotubes coated with yttria. *Appl. Phys. Lett.* **2006**, *88*, 143104 (1−3).
(24) Loitongbam, R. S.; Singh, N. S.; Singh, W. R.; Ningthoujam, R. S. Observation of exceptional strong emission transitions ^5D_j (j = 1−3) to ^7F_j (j = 1−3): multicolor from single Eu^{3+} ion doped La_2O_3 nanoparticles. *J. Lumin.* **2013**, *134*, 14−23.
(25) Vetrone, F.; Naccache, R.; Mahalingam, V.; Morgan, C. G.; Capobianco, J. A. The active-core/active-shell approach: a strategy to enhance the upconversion luminescence in lanthanide-doped nanoparticles. *Adv. Funct. Mater.* **2009**, *19*, 2924−2929.
(26) Singh, N. S.; Ningthoujam, R. S.; Phaomei, G.; Singh, S. D.; Vinu, A.; Vatsa, R. K. Re-dispersion and film formation of $GdVO_4$:Ln^{3+} (Ln^{3+} = Dy^{3+}, Eu^{3+}, Sm^{3+}, Tm^{3+}) nanoparticles: particle size and luminescence studies. *Dalton Trans.* **2012**, *41*, 4404−4412.
(27) Luwang, M. N.; Ningthoujam, R. S.; Jagannath; Srivastava, S. K.; Vatsa, R. K. Effects of Ce^{3+} codoping and annealing on phase transformation and luminescence of Eu^{3+}-Doped YPO_4 nanorods: D_2O solvent effect. *J. Am. Chem. Soc.* **2010**, *132*, 2759−2768.
(28) Yang, M.; You, H.; Liu, K.; Zheng, Y.; Guo, N.; Zhang, H. Low-temperature coprecipitation synthesis and luminescent properties of $LaPO_4$:Ln^{3+} (Ln^{3+} = Ce^{3+}, Tb^{3+}) nanowires and $LaPO_4$:Ce^{3+},Tb^{3+}/$LaPO_4$ core/shell nanowires. *Inorg. Chem.* **2010**, *49*, 4996−5002.
(29) Wu, C.-C.; Chen, K.-B.; Lee, C.-S.; Chen, T.-M.; Cheng, B.-M. Synthesis and VUV photoluminescence characterization of (Y,Gd)-(V,P)O_4:Eu^{3+} as a potential red-emitting PDP phosphor. *Chem. Mater.* **2007**, *19*, 3278−3285.
(30) Parchur, A. K.; Ningthoujam, R. S. Preparation and structure refinement of Eu^{3+} doped $CaMoO_4$ nanoparticles. *Dalton Trans.* **2011**, *40*, 7590−7594.
(31) Lisiecki, R.; Solarz, P.; Dominiak-Dzik, G.; Ryba-Romanowski, W.; Sobczyk, M.; Cerny, P.; Sulc, J.; Jelinkova, H.; Urata, Y.; Higuchi, M. Comparative optical study of thulium-doped YVO_4, $GdVO_4$, and $LuVO_4$ single crystals. *Phys. Rev. B* **2006**, *74*, 035103 (1−14).
(32) Chen, D.; Yu, Y.; Huang, P.; Lin, H.; Shan, Z.; Zeng, L.; Yang, A.; Wang, Y. Color-tunable luminescence for Bi^{3+}/Ln^{3+}:YVO_4 (Ln = Eu, Sm, Dy, Ho) nanophosphors excitable by near-ultraviolet light. *Phys. Chem. Chem. Phys.* **2010**, *12*, 7775−7778.
(33) Singh, N. S.; Ningthoujam, R. S.; Luwang, M. N.; Singh, S. D.; Vatsa, R. K. Luminescence, lifetime and quantum yield studies of YVO_4:Ln^{3+} (Ln^{3+} = Dy^{3+}, Eu^{3+}) nanoparticles: concentration and annealing effects. *Chem. Phys. Lett.* **2009**, *480*, 237−242.
(34) Ren, W.; Tian, G.; Zhou, L.; Yin, W.; Yan, L.; Jin, S.; Zu, Y.; Li, S.; Gu, Z.; Zhao, Y. Lanthanide ion-doped $GdPO_4$ nanorods with dual-modal bio-optical and magnetic resonance imaging properties. *Nanoscale* **2012**, *4*, 3754−3760.
(35) Phaomei, G.; Ningthoujam, R. S.; Singh, W. R.; Loitongbam, R. S.; Singh, N. S.; Rath, A.; Juluri, R. R.; Vatsa, R. K. Luminescence switching behavior through redox reaction in Ce^{3+} co-doped $LaPO_4$:Tb^{3+} nanorods: re-dispersible and polymer film. *Dalton Trans.* **2011**, *40*, 11571−11580.
(36) Wang, L.; Zhou, C. L.; Chen, H. Q.; Chen, J. G.; Fu, J.; Ling, B. Determination of formaldehyde in aqueous solutions by a novel fluorescence energy transfer system. *Analyst* **2010**, *135*, 2139−2143.
(37) Caravan, P.; Ellison, J. J.; McMurry, T. J.; Lauffer, R. B. Gadolinium(III) chelates as MRI contrast agents: structure, dynamics, and applications. *Chem. Rev.* **1999**, *99*, 2293−2352.
(38) Johnson, N. J. J.; Oakden, W.; Stanisz, G. J.; Prosser, R. S.; van Veggel, F. C. J. M. Size-tunable, ultrasmall $NaGdF_4$ nanoparticles: insights into their T_1 MRI contrast enhancement. *Chem. Mater.* **2011**, *23*, 3714−3722.
(39) Cheung, E. N. M.; Alvares, R. D. A.; Oakden, W.; Chaudhary, R.; Hill, M. L.; Pichaandi, J.; Mo, G. C. H.; Yip, C.; Macdonald, P. M.; Stanisz, G. J.; van Veggel, F. C. J. M.; Prosser, R. S. Polymer-stabilized lanthanide fluoride nanoparticle aggregates as contrast agents for magnetic resonance imaging and computed tomography. *Chem. Mater.* **2010**, *22*, 4728−4739.
(40) Shannon, R. D. Revised effective ionic radii and systematic studies of interatomic distances in halides and chalcogenides. *Acta Crystallogr. A* **1976**, *32*, 751−767.
(41) Nakamoto, K. *Infrared and Raman Spectra of Inorganic and Coordination Compounds*, 5th ed.; Wiley: New York, USA, 1986.
(42) Sudhakar, N.; Ningthoujam, R. S.; Rajeev, K. P.; Nigam, A. K.; Weissmüller, J.; Gajbhiye, N. S. Effect of La, B doping on the electrical resistivity and magnetic susceptibility of nanocrystalline vanadium nitride. *J. Appl. Phys.* **2004**, *96*, 688−695.

(43) Ningthoujam, R. S. *Enhancement of Photoluminescence by Rare Earth Ions Doping in Semiconductor Inorganic*; Rai, S. B., Dwivedi, Y., Eds.; Nova Science Publishers Inc.: USA, 2012.
(44) Dexter, D. L. A theory of sensitized luminescence in solids. *J. Chem. Phys.* **1953**, *21*, 836−850.
(45) Lakowicz, J. R. *Principles of Fluorescence Spectroscopy*; Kluwer Academic/Plenum Publishers: New York, 1999; p 131.
(46) Yaiphaba, N.; Ningthoujam, R. S.; Singh, N. R.; Vatsa, R. K. Luminescence properties of redispersible Tb^{3+}-doped $GdPO_4$ nanoparticles prepared by an ethylene glycol route. *Eur. J. Inorg. Chem.* **2010**, *18*, 2682−2687.
(47) Xia, Z. G.; Liu, R. S. Tunable blue-green color emission and energy transfer of $Ca_2Al_3O_6F:Ce^{3+},Tb^{3+}$ phosphors for near-UV white LEDs. *J. Phys. Chem. C* **2012**, *116*, 15604−15609.
(48) Kitsuda, M.; Fujihara, S. Quantitative luminescence switching in $CePO_4$:Tb by redox reactions. *J. Phys. Chem. C* **2011**, *115*, 8808−8815.
(49) Melhuish, W. H. Modified technique for determining the wavelength-sensitivity curve of a spectrofluorimeter. *Appl. Opt.* **1975**, *14*, 26−27.